Journal of the Mechanics and Physics of Solids 125 (2019) 736–748

Contents lists available at ScienceDirect

Journal of the Mechanics and Physics of Solids

journal homepage: www.elsevier.com/locate/jmps

Mechanics of buckled serpentine structures formed via mechanics-guided, deterministic three-dimensional assembly

Shupeng Li[a,b], Mengdi Han[c], John A. Rogers[c,d,e,f], Yihui Zhang[a], Yonggang Huang[b,c,d,e,*], Heling Wang[b,d,e,*]

[a] Center for Flexible Electronics Technology and Center for Mechanics and Materials; AML, Department of Engineering Mechanics, Tsinghua University, Beijing, China
[b] Departments of Civil and Environmental Engineering, Northwestern University, Evanston, IL, USA
[c] Center for Bio-Integrated Electronics, Northwestern University, Evanston, IL, USA
[d] Department of Mechanical Engineering, Northwestern University, Evanston, IL, USA
[e] Department of Materials Science and Engineering, Northwestern University, Evanston, IL, USA
[f] Department of Biomedical Engineering, Neurological Surgery, Chemistry, Electrical Engineering and Computer Science; Simpson Querrey Institute for Bio-Nanotechnology, and Center for Advanced Regenerative Engineering, Northwestern University, Evanston, IL, USA

ARTICLE INFO

Article history:
Received 29 December 2018
Accepted 27 January 2019
Available online 29 January 2019

Keywords:
Buckled serpentine structures
Mechanics-guided
Deterministic 3D assembly
Stretchable electronics
Phase diagram
Scaling law

ABSTRACT

Many forms of stretchable electronic systems incorporate planar, filamentary serpentine structures to realize high levels of stretchability in ways that allow the use of high performance of inorganic functional materials. Recent advances in mechanics-guided, deterministic three-dimensional (3D) assembly provide routes to transform these traditional, two-dimensional (2D) serpentine layouts into 3D architectures, with significantly improved mechanics and potential for applications in energy harvesters, pressure sensors, soft robotics, biomedical devices and other classes of technologies. One challenge is that, by comparison to other geometries, the relatively low bending stiffnesses of the serpentine structures create difficulties in overcoming the interfacial adhesion energy to allow delamination from the underlying elastomeric substrate, as an essential aspect of the assembly process. An additional complication is that many of the functional materials widely used in stretchable electronics have a low strain threshold for failure such that damage can occur during buckling-induced assembly. Therefore, a clear understanding of the mechanics of buckled serpentine structures is essential to their design, fabrication and application. Through theoretical modeling and finite element analysis, we present models for the phase diagram of buckled states and the maximum strain in the globally-buckled serpentine structures. The analysis yield formulae in concise and explicit forms, clearly showing the effect of geometry/material parameters and the prestrain. The results can be used in designing buckled serpentine structures to ensure their compatibility with the mechanics-guided, deterministic 3D assembly and facilitate their applications in stretchable electronics.

1. Introduction

Serpentine structures have wide applications in flexible and stretchable electronics, as they provide a rich range of design options to achieve unusually high levels of stretchability while maintaining high performance operation (Khang et al., 2006;

* Corresponding authors at: Departments of Civil and Environmental Engineering, Northwestern University, Evanston, IL, USA.
E-mail addresses: y-huang@northwestern.edu (Y. Huang), helingwang1@gmail.com (H. Wang).

https://doi.org/10.1016/j.jmps.2019.01.019
0022-5096/

Xu et al., 2013; Fan et al., 2014; Gutruf et al., 2014; Lu and Kim, 2014; Xu et al., 2014; Mamidanna et al., 2016; Huang et al., 2017; Ma et al., 2017a; Pan et al., 2017; Su et al., 2017; Alcheikh et al., 2018; Cui et al., 2018a; Zhao et al., 2018). Such structures can be used in devices for energy conversion and storage (Xu et al., 2013; Yang et al., 2015; Lai et al., 2017), in diagnostic and therapeutic biomedical devices (Son et al., 2014; Lin et al., 2016; Gao et al., 2017a; Liu et al., 2017; Nyein et al., 2018), in human-machine interfaces (Dong et al., 2018a, 2018b), and in general forms of electronics (Lu et al., 2012; Han et al., 2016; Gao et al., 2017b; Ma et al., 2017b; Hu et al., 2018; Yang et al., 2018) and optoelectronics (Park et al., 2015; Dai et al., 2016; Vásquez Quintero et al., 2017; Gutruf et al., 2018). Serpentine structures in such applications are mostly two-dimensional (2D) in their layouts. Recent studies show that three dimensional (3D) structures, especially those integrated with functional components, are of emerging utility as 3D vibrational platforms (Ning et al., 2017; Li et al., 2018a; Wang et al., 2018) for fluid mechanics (Ning et al., 2018a) and polymer mechanics (Nan et al., 2018a) studies, as thermoelectric/mechanical/solar energy harvesters (Ahn et al., 2009; Nan et al., 2018b; Han et al., 2019), strain/temperature/electrophysiological sensors (Zarek et al., 2016; Guo et al., 2018a), soft robotic components (Wehner et al., 2016; Kim et al., 2018a) and biomedical devices (Wu et al., 2011; Sun et al., 2012; Kolesky et al., 2014; Han et al., 2016; Skylar-Scott et al., 2016; Zhu and Cheng, 2018). Mechanics-guided, deterministic approaches in 3D assembly can transform well-defined 2D precursors into complex, but well controlled 3D shapes (Sun et al., 2006; Xu et al., 2015; Zhang et al., 2015; Yan et al., 2016; Liao et al., 2017; Fu et al., 2017; Zhang et al., 2017; Cui et al., 2018b; Fu et al., 2018; Yu et al., 2018) with the ability to integrate diverse functional materials such as piezoelectric membranes (Ning et al., 2018a), doped single-crystalline silicon (Kim et al., 2018b), metals (Jang et al., 2017; Yan et al., 2017; Kim et al., 2018c; Nan et al., 2018a; Zhang et al., 2019), shape memory polymers (Guo et al., 2018b; Ning et al., 2018b; Wang et al., 2019) and elastomers (Mao et al., 2017; Li et al., 2018b). Based on these techniques, Han et al. (2019) formed buckled serpentine structures made of a piezoelectric polymer. Because of their ultra-low stiffnesses and buckled 3D shapes, these structures can operate as low frequency, broad band energy harvesters and sensors. However, their unique geometries and ultra-low stiffnesses also raise two questions about the straightforward realization of such structures via the mechanics-guided, deterministic 3D assembly technique.

1) Can the serpentine structures overcome the adhesion energy with the underlying elastomeric substrate to buckle into the 3D shape? In mechanics-guided, deterministic 3D assembly, only a selected part of the 2D precursor bonds strongly to the substrate, while the other parts only weakly adhere, most typically by Van der Waals forces. Results of Wang et al. (2010) suggest that the prestrain of the substrate must exceed a critical value for these weakly adhered regions to fully delaminate from the substrate (global-buckling) during the assembly process. For small prestrain, test structures such as straight ribbons only partially delaminate (local-buckling) or entirely adhere to the substrate (no-buckling). Mechanics-guided, deterministic 3D assembly relies on global buckling state. Compared with a straight ribbon, a serpentine structure has an even smaller bending stiffness and is therefore even more difficult to delaminate from the substrate because of the reduced strain energy compared with the adhesion energy. Although adding a temporary sacrificial layer below the serpentine structure may facilitate the buckling process (Han et al., 2019), this strategy significantly increases the complexity and difficulty of fabrication. Theoretical models reported in literature mainly focus on buckling of structures in relatively simple geometries (Wang et al., 2010; Wang and Wang, 2016). The model in Wang et al. (2010) predict the phase diagram of a buckled single ribbon under compression, but the model cannot be applied or generalized directly to the serpentine structure, due to its complex geometry.
2) Is the strain in the buckled serpentine structure sufficiently small to avoid failure? Many functional materials in electronics have a low strain threshold for failure, e.g. yield strain of gold is 0.3%; fracture limits of PZT and silicon are 0.6% (Cao and Evans, 1993; Guillon et al., 2002) and $<$2% (Vedde and Gravesen, 1996), respectively. Many models exist the deformations and strains of 2D serpentine structures (Zhang et al., 2013; Shi et al., 2014; Zhang et al., 2014a; Zhang et al., 2014b; Fu et al., 2015; Lu and Yang, 2015; Ma and Zhang, 2016; Wang et al., 2017; Chen et al., 2018), and some apply also to buckled structures in simple shapes such as arches (Xiao et al., 2008; Su et al., 2012; Xue et al., 2018; Zhou et al., 2018; Coupean *et al.*, 2019) and helical coils (Chen et al., 2016; Liu et al., 2016; Fan et al., 2018). However, the above models are not directly applicable to buckled serpentine structures.

Therefore, a theoretical model for the buckled serpentine structures is necessary and important to guide the design and fabrication. Here we present a study through theoretical modeling and finite element analysis (FEA). The results yield formulae in very concise forms to predict the phase diagram of buckled states (no buckling, local buckling and global buckling), as well as the maximum strain in the globally-buckled serpentine structure.

2. Buckling of serpentine structures

Fig. 1a shows the geometric parameters of a 2D precursor of the serpentine structure, which is adhered to a pre-stretched elastomeric substrate (Fig. 1b). The two ends of the 2D precursor are chemically treated such that they form strong bonds with the substrate, while the other parts are weakly adhered to the substrate via the van der walls force (Zhang et al., 2015). Following the complete release of substrate prestrain, the 2D precursor is under compression from the substrate, and may buckle up if the prestrain exceeds a threshold. Fig. 1c, d, and e show three representative deformed states: the

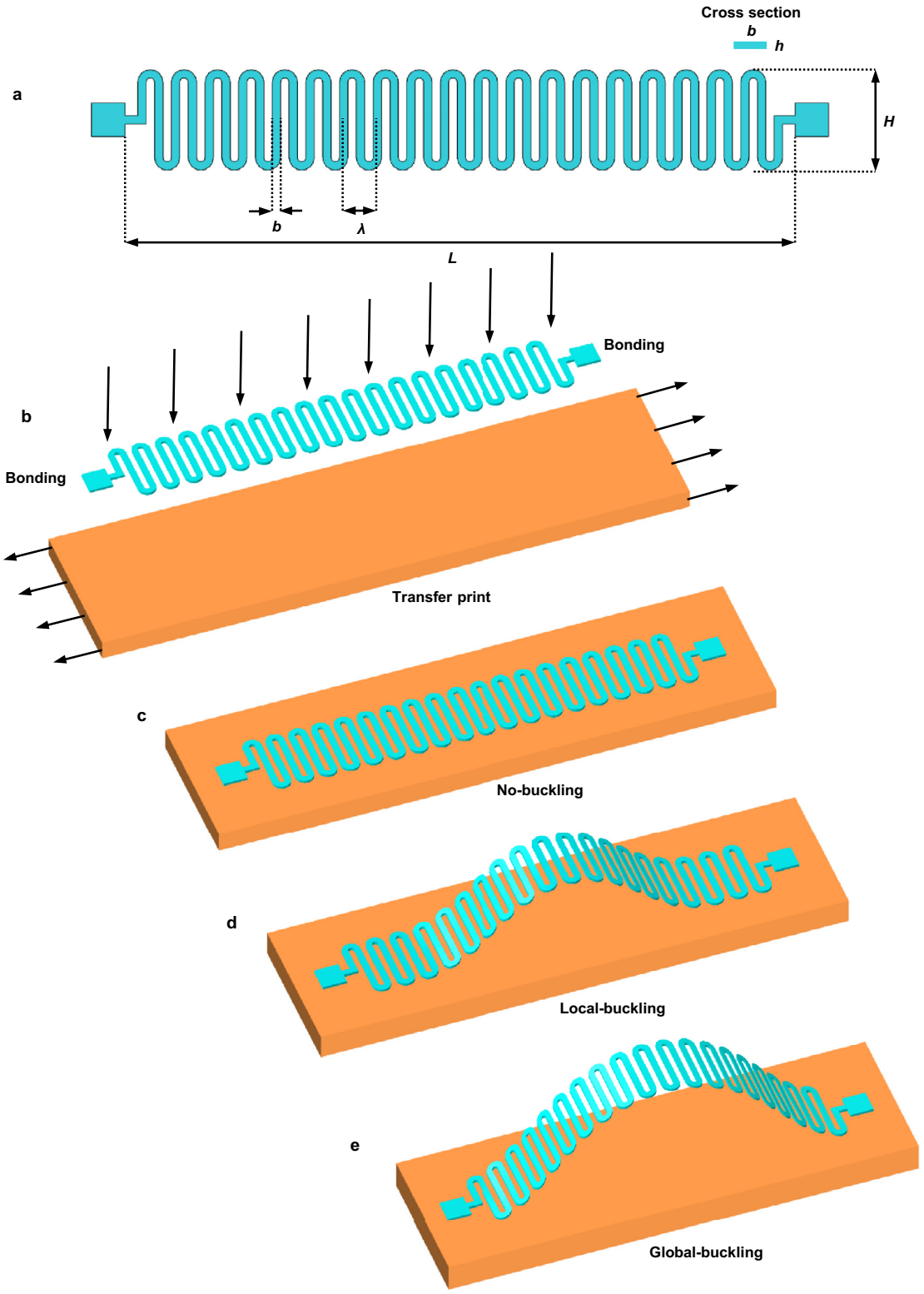

Fig. 1. Schematic illustrations of a serpentine structure on a pre-stretched elastomeric substrate, and the buckled serpentine after the prestrain release in the substrate. (a) The geometric parameters of the serpentine structure, (b) transfer print of serpentine structure onto a pre-stretched elastomer substrate, (c) the no-buckling state after release of a small prestrain, (d) the local-buckling state after release of an intermediate prestrain, and (e) the global-buckling state after release of a large prestrain.

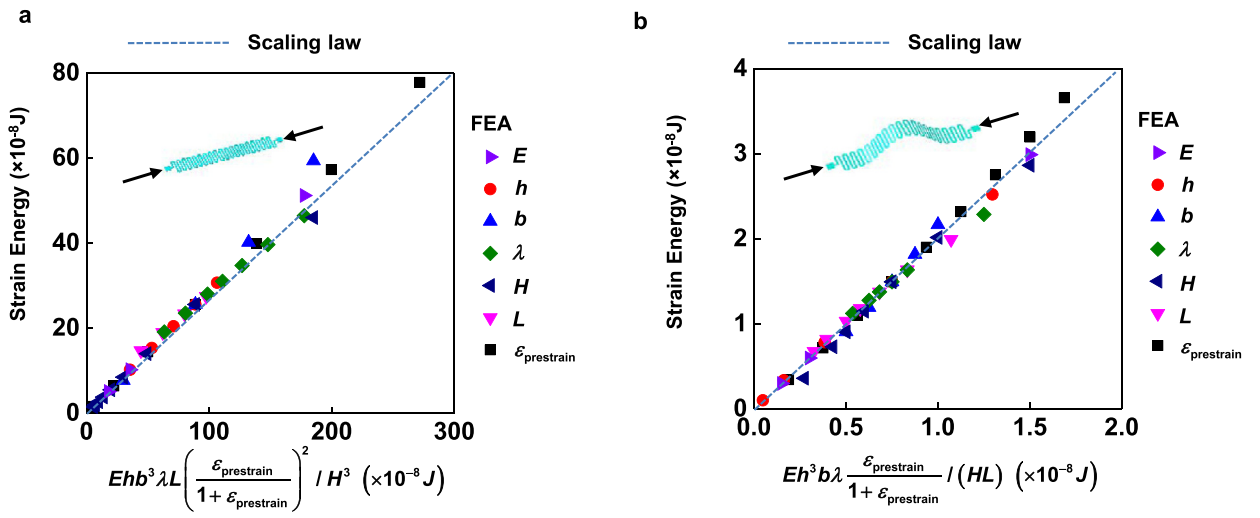

Fig. 2. Scaling laws and FEA results for the strain energy of the (a) no-buckling and (b) global-buckling states for the baseline values of thickness Young's modulus $E = 2.5$ GPa, thickness $h = 10\,\mu$m, width $b = 60\,\mu$m, unit cell length $\lambda = 200\,\mu$m, height $H = 400\,\mu$m, representative length $L = 2000\,\mu$m, and prestrain $\varepsilon_{\text{prestrain}} = 0.25$, and each of the 7 parameters varies independently in its representative range.

no-buckling state[1] (no delamination, Fig. 1c) at small prestrain, the local-buckling state (partial delamination of the weak bonding, Fig. 1d) at intermediate prestrain, and the global-buckling state (complete delamination of the weak bonding, Fig. 1e) at large prestrain. In the following the total energy for each state is obtained in terms of the prestrain, serpentine geometries and material properties.

2.1. No-buckling state

The total energy for the no-buckling state (Fig. 1c) is the strain energy of the flat serpentine under compression because the strain energy in the substrate is negligible upon the complete release of the substrate prestrain, which results in the compression $\frac{\varepsilon_{\text{prestrain}}}{1+\varepsilon_{\text{prestrain}}}$ on the serpentine, where $\varepsilon_{\text{prestrain}}$ is the substrate prestrain. The strain energy in the serpentine is linearly proportional to the representative length L and Young's modulus E of serpentine ribbon, and to the square of compression $(\frac{\varepsilon_{\text{prestrain}}}{1+\varepsilon_{\text{prestrain}}})^2$ since the deformation is linear elastic prior to buckling. In addition, prior to buckling the serpentine is mainly subjected to in-plane bending, and its (in-plane) bending stiffness is $\frac{hb^3}{12}$, which is much larger than the out-of-plane bending stiffness $\frac{bh^3}{12}$ since the ribbon thickness h (in the normal direction of the substrate), in general, is much smaller than the ribbon width b, i.e., $h \ll b$. Therefore the strain energy in the serpentine is linearly proportional to Ehb^3, and the total energy of the no-buckling state takes the form

$$W_{\text{no}} \propto Ehb^3 L\left(\frac{\varepsilon_{\text{prestrain}}}{1+\varepsilon_{\text{prestrain}}}\right)^2. \tag{1}$$

The total energy above also depends on parameters pertinent to the serpentine, namely the serpentine height H and unit cell length λ (Fig. 1a), where λ, in general, is much smaller than the representative length L of the serpentine, i.e., $\lambda \ll L$. The FEA suggests that the total energy is linearly proportional to λ and inversely proportional to H^3, and is given by

$$W_{\text{no}} = 0.26\frac{Ehb^3\lambda L}{H^3}\left(\frac{\varepsilon_{\text{prestrain}}}{1+\varepsilon_{\text{prestrain}}}\right)^2. \tag{2}$$

This equation has been validated via FEA by the commercial software ABAQUS with its four-node reduced integration finite-strain shell elements (S4R), and at least 8 elements along the ribbon width to ensure the accuracy. Eq. (2) involves 7 parameters: 5 for the serpentine geometry (h, b, λ, L, and H), Young's modulus and pre-strain. Fig. 2a shows W_{no} versus the combination of these 7 parameters $\frac{Ehb^3\lambda L}{H^3}(\frac{\varepsilon_{\text{prestrain}}}{1+\varepsilon_{\text{prestrain}}})^2$; the straight line corresponds to Eq. (2) and its slope is 0.26; the dots are for FEA with the baseline values of 7 parameters $E = 2.5$ GPa, $h = 10\,\mu$m, $b = 60\,\mu$m, $\lambda = 200\,\mu$m, $H = 400\,\mu$m, $L = 2000\,\mu$m, and $\varepsilon_{\text{prestrain}} = 0.25$, and each of the 7 parameters varies independently in its representative range. It is clear that Eq. (2) is

[1] In this no-buckling state the serpentine structure does not delaminate from the substrate, but it may wrinkle once the prestrain exceeds a critical value (Khang et al., 2006). However, the wrinkle disappears once delamination starts, as observed in the numerical simulations and also experiments (Vella et al., 2009). Therefore, the state of wrinkling is not considered in this paper.

quite accurate for the total energy W_{no} of the no-buckling state. The Poisson's ratio of the serpentine ribbon has negligible effect (<0.1%) on W_{no}.

2.2. Global-buckling state

For global buckling, the serpentine structure delaminates from the substrate except for the strong bonding (Fig. 1d). Its total energy consists of the following two parts.

1) The adhesion energy $\gamma S\frac{L}{\lambda}$, where γ is the work of adhesion between the serpentine and the substrate, $S=(\frac{\pi}{2}-1)b\lambda+2bH+2b^2$ is the area of one unit cell of the serpentine structure, and $\frac{L}{\lambda}$ is the number of total number of unit cells.
2) The strain energy in the buckled serpentine, which is linearly proportional to the out-of-plane bending stiffness $\frac{Eh^3b}{12}$ of the serpentine ribbon. It is also linearly proportional to the compression $\frac{\varepsilon_{\text{prestrain}}}{1+\varepsilon_{\text{prestrain}}}$ because the nonlinear post-buckling deformation is proportional to the square root of compression (Su et al., 2012a)[2]. Therefore, the strain energy in the buckled serpentine is $\propto \frac{Eh^3b}{L}\frac{\varepsilon_{\text{prestrain}}}{1+\varepsilon_{\text{prestrain}}}$. Here the $\propto \frac{1}{L}$ term results from the bending energy, which scales linearly with the representative length L and the square of curvature κ of the serpentine, and κ is inversely proportional to L. This $\propto \frac{1}{L}$ scaling has also been observed in buckling of straight ribbons (Wang et al., 2010). FEA suggests that the strain energy is linearly proportional to the unit cell length λ and inversely proportional to the serpentine height H, and is given by $2.0\frac{Eh^3b\lambda}{HL}\frac{\varepsilon_{\text{prestrain}}}{1+\varepsilon_{\text{prestrain}}}$. As shown in Fig. 2b, this formula has been validated via FEA for the same baseline values and the same range of those 7 parameters as in Fig. 2a. The straight line and dots in Fig. 2b, corresponding to the above formula and FEA, respectively, agree very well. The slope of the straight line is 2.0, which is obtained for the Poisson's ratio 0.34 (for Polyimide). This slope has a weak dependence (a few percent) on the Poisson's ratio. The total energy of the global-buckling state is then given by

$$W_{\text{global}}=2.0\frac{Eh^3b\lambda}{HL}\frac{\varepsilon_{\text{prestrain}}}{1+\varepsilon_{\text{prestrain}}}+\gamma S\frac{L}{\lambda}. \tag{3}$$

2.3. Local-buckling state

For local buckling, the serpentine structure partially delaminates from the substrate (Fig. 1e), and its representative length of delamination is denoted by L–l, where l (to be determined) is the representative length of the serpentine that remains adhered to the substrate. The limits of $l=0$ and $l=L$ correspond to the global- and no-buckling states, respectively. Let ε_1 and ε_2 denote the average compressions over the buckled (delaminated) and no-buckling (flat) parts of the serpentine, respectively, and they are related by

$$\varepsilon_1(L-l)+\varepsilon_2 l=\frac{\varepsilon_{\text{prestrain}}}{1+\varepsilon_{\text{prestrain}}}L. \tag{4}$$

The total energy consists of the following three parts.

1) The strain energy of the no-buckling part, which is obtained from Eq. (2) by replacing L and $\frac{\varepsilon_{\text{prestrain}}}{1+\varepsilon_{\text{prestrain}}}$ with l and ε_2, respectively, to give $0.26\frac{Ehb^3\lambda l}{H^3}\varepsilon_2^2$.
2) The adhesion energy of the buckled (delaminated) part, which is obtained from $\gamma S\frac{L}{\lambda}$ in Eq. (3) by replacing L with L–l, to give $\gamma S\frac{L-l}{\lambda}$.
3) The strain energy of the buckled serpentine[3], which is obtained from $2.0\frac{Eh^3b\lambda}{HL}\frac{\varepsilon_{\text{prestrain}}}{1+\varepsilon_{\text{prestrain}}}$ in Eq. (3) by replacing L and $\frac{\varepsilon_{\text{prestrain}}}{1+\varepsilon_{\text{prestrain}}}$ with L–l and ε_1, respectively, to give $2.0\frac{Eh^3b\lambda}{H(L-l)}\varepsilon_1$.

The total energy of the local-buckling state is then given by

$$\begin{aligned}W_{\text{local}}&=0.26\frac{Ehb^3\lambda l}{H^3}\varepsilon_2^2+2.0\frac{Eh^3b\lambda}{H(L-l)}\varepsilon_1+\gamma S\frac{L-l}{\lambda}\\&=0.26\frac{Ehb^3\lambda l}{H^3}\varepsilon_2^2+2.0\frac{Eh^3b\lambda}{H(L-l)^2}\left(\frac{\varepsilon_{\text{prestrain}}}{1+\varepsilon_{\text{prestrain}}}L-\varepsilon_2 l\right)+\gamma S\frac{L-l}{\lambda},\end{aligned} \tag{5}$$

where Eq. (4) is used to eliminate ε_1. Minimization of W_{local} in Eq. (5) with respect to ε_2 gives

$$\varepsilon_2=3.8\frac{h^2H^2}{b^2(L-l)^2}. \tag{6}$$

[2] The post-buckling deformation is linearly proportional to $\sqrt{\varepsilon-\varepsilon_c}$ where ε is the compression, and ε_c is the critical value for the onset of buckling. In general, ε_c is very small (a fraction of a percent) so that the post-buckling deformation is $\propto\sqrt{\varepsilon}$ and the strain energy is $\propto\varepsilon$.

[3] It can be shown analytically that the total energy for multiple partial delaminations is higher than that for a single partial delamination, and is not considered in this study.

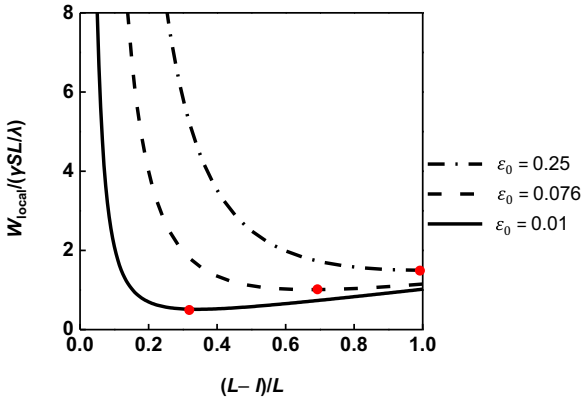

Fig. 3. The normalized total energy of the local-buckling state versus the normalized delamination length $(L–l)/L$ with different normalized compression ε_0. The dots denote the minimal energy.

Its substitution into Eq. (5) yields

$$W_{\text{local}} = -3.8\frac{Eh^5\lambda Hl}{b(L-l)^4} + 2.0\frac{Eh^3b\lambda L}{H(L-l)^2}\frac{\varepsilon_{\text{prestrain}}}{1+\varepsilon_{\text{prestrain}}} + \gamma S\frac{L-l}{\lambda}. \tag{7}$$

It should be pointed out, for $h \ll b$, $H \ll L$ and pre-strain $\varepsilon_{\text{prestrain}}$ not vanishingly small, the first term on the right hand side of the above equation becomes negligible as compared to the second term (See Appendix A for details). Eq. (7) can then be well approximated by

$$W_{\text{local}} \approx 2.0\frac{Eh^3b\lambda L}{H(L-l)^2}\frac{\varepsilon_{\text{prestrain}}}{1+\varepsilon_{\text{prestrain}}} + \gamma S\frac{L-l}{\lambda}. \tag{8}$$

Fig. 3 shows the normalized total energy of the local-buckling state $\frac{W_{\text{local}}}{\gamma S\frac{L}{\lambda}}$, versus the normalized delamination length $(L–l)/L$ for the normalized compression

$$\varepsilon_0 = \frac{Eh^3b\lambda^2}{\gamma HSL^2}\frac{\varepsilon_{\text{prestrain}}}{1+\varepsilon_{\text{prestrain}}} \tag{9}$$

$= 0.01$, 0.076 and 0.25, and the medium value $\varepsilon_0 = 0.076$ corresponds to baseline values of those 7 parameters and $\gamma = 0.16$ N/m. The energy W_{local} reaches the minimum when the delamination length $L–l$ is 0.34 L, 0.67 L and L for $\varepsilon_0 = 0.01$, 0.076 and 0.25, respectively. Here $\varepsilon_0 = 0.25$ corresponds to the complete delamination $l = 0$ (i.e., global buckling).

In general, the delamination length $L–l$ can be determined by minimizing W_{local} with respect to $L–l$ as

$$L-l = \sqrt[3]{\frac{4Eh^3b\lambda^2L}{\gamma HS}\frac{\varepsilon_{\text{prestrain}}}{1+\varepsilon_{\text{prestrain}}}} = \sqrt[3]{4\varepsilon_0}L. \tag{10}$$

Its limit $l = 0$ gives the maximum compression for local buckling, i.e., $\varepsilon_0 \le \frac{1}{4}$, beyond which local buckling does not occur. Substitution of Eq. (10) into Eq. (8) gives

$$W_{\text{local}} = \frac{3}{2}\sqrt[3]{\frac{4E\gamma^2h^3bS^2L}{\lambda H}\frac{\varepsilon_{\text{prestrain}}}{1+\varepsilon_{\text{prestrain}}}} = 3\sqrt[3]{\frac{\varepsilon_0}{2}}\gamma S\frac{L}{\lambda}, \tag{11}$$

for $\varepsilon_0 \le \frac{1}{4}$.

2.4. The phase diagram of buckling states

The total energy for no-, local- and global-buckling states in Eqs. (2), (11) and (3), respectively, can be expressed in terms of ε_0 as

$$\frac{W_{\text{no}}}{\gamma S\frac{L}{\lambda}} = 0.26\gamma'\varepsilon_0^2, \quad \frac{W_{\text{local}}}{\gamma S\frac{L}{\lambda}} = 3\sqrt[3]{\frac{\varepsilon_0}{2}}, \quad \frac{W_{\text{global}}}{\gamma S\frac{L}{\lambda}} = 2\varepsilon_0 + 1, \tag{12}$$

where $\gamma' = \frac{\gamma bSL^4}{Eh^5\lambda^2H}$ represents the adhesion energy normalized by the elastic modulus E and combination of geometry parameters of the serpentine. The total energy for each state (i.e., no-, local- and global-buckling) given in Eq. (12) is shown versus ε_0 in Fig. 4a for relatively strong adhesion $\gamma' = 1.5 \times 10^4$. It is clear that, as ε_0 increases, the state changes from

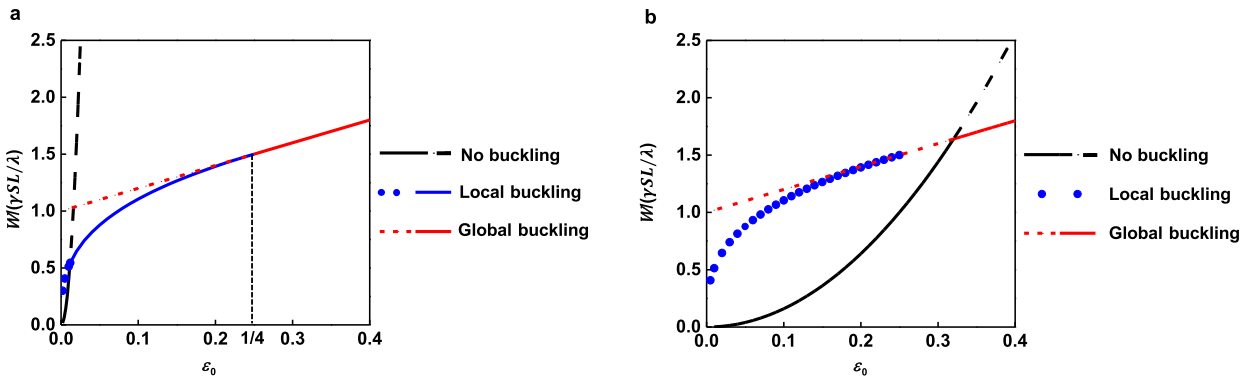

Fig. 4. The normalized total energy versus the normalized compression ε_0 for the no-, local- and global-buckling states (a) strong adhesion γ'=1.5 × 10^4 and (b) relatively weak adhesion γ'= 62.

no-buckling to local-buckling and eventually to global-buckling. For each ε_0, the total energy of the system is the minimal of those in Eq. (12), i.e.,

$$W = \min\left(W_{\text{no}}, W_{\text{local}}, W_{\text{global}}\right), \tag{13}$$

and is represented by the solid line in Fig. 4a. For relatively strong adhesion $\gamma' > 92$, the total energy in Eq. (13) is given explicitly as

$$W = \begin{cases} W_{\text{no}} & 0 < \varepsilon_0 < \sqrt[5]{\frac{770}{\gamma'^3}} \\ W_{\text{local}} & \sqrt[5]{\frac{770}{\gamma'^3}} < \varepsilon_0 < \frac{1}{4} \\ W_{\text{global}} & \varepsilon_0 > \frac{1}{4} \end{cases} \text{ for } \gamma' > 92, \tag{14}$$

where the critical normalized compression $\sqrt[5]{\frac{770}{\gamma'^3}}$ separating the no- and local-buckling states is obtained from $W_{\text{no}} = W_{\text{local}}$, and the critical normalized compression separating the local- and global-buckling states is $\frac{1}{4}$. For relatively weak adhesion$\gamma' < 92$, the total energy in Eq. (13) becomes

$$W = \begin{cases} W_{\text{no}} & 0 < \varepsilon_0 < \frac{3.8}{\gamma'} + \sqrt{\frac{15}{\gamma'^2} + \frac{3.8}{\gamma'}} \\ W_{\text{global}} & \varepsilon_0 > \frac{3.8}{\gamma'} + \sqrt{\frac{15}{\gamma'^2} + \frac{3.8}{\gamma'}} \end{cases}, \text{ for } \gamma' < 92, \tag{15}$$

where the critical normalized compression $\frac{3.8}{\gamma'} + \sqrt{\frac{15}{\gamma'^2} + \frac{3.8}{\gamma'}}$ separating the no- and global-buckling states is obtained from $W_{\text{no}} = W_{\text{global}}$. It is important to point out that, for relatively weak adhesion $\gamma' < 92$, the state changes from no-buckling to global-buckling directly, without local-buckling. This is illustrated in Fig. 4b, where the total energy for each state (i.e., no-, local- and global-buckling) given in Eq. (12) is shown versus ε_0 for $\gamma' = 62$. The solid line represents the total energy of the system given in Eq. (13). The curve for the local-buckling is always higher than those of no- or global-buckling.

Fig. 5 shows the phase diagram of the buckling states, i.e., the normalized compression ε_0 versus the normalized adhesion energy γ', where the domains for no-, local- and global-buckling are clearly marked. It once again shows that, for relatively weak adhesion $\gamma' = \frac{\gamma bSL^4}{Eh^5\lambda^2 H} < 92$, the no-buckling state changes to the global-buckling state directly as the compression (or equivalently, the prestrain) increases. For relatively strong adhesion $\gamma' = \frac{\gamma bSL^4}{Eh^5\lambda^2 H} > 92$, the no-buckling states goes through the local-buckling state and eventually reaches the global-buckling state as the compression (prestrain) increases. These are summarized in Table 1, where the range of prestrain for each state is clearly given.

Table 1
The range of prestrain for no-, local- and global-buckling states.

	Strong adhesion $\frac{\gamma bSL^4}{Eh^5\lambda^2 H} > 92$	Weak adhesion $\frac{\gamma bSL^4}{Eh^5\lambda^2 H} < 92$
No buckling	$\frac{\varepsilon_{\text{prestrain}}}{1+\varepsilon_{\text{prestrain}}} < \sqrt[5]{770\,\frac{\gamma^2 H^8 S^2}{E^2 b^8 \lambda^4 L^2}}$	$\frac{\varepsilon_{\text{prestrain}}}{1+\varepsilon_{\text{prestrain}}} < 3.8\frac{h^2H^2}{b^2L^2} + \sqrt{15\frac{h^4H^4}{b^4L^4} + 3.8\frac{\gamma H^3 S}{Ehb^3\lambda^2}}$
Local buckling	$\sqrt[5]{770\,\frac{\gamma^2 H^8 S^2}{E^2 b^8 \lambda^4 L^2}} < \frac{\varepsilon_{\text{prestrain}}}{1+\varepsilon_{\text{prestrain}}} < \frac{\gamma HSL^2}{4Eh^3 b\lambda^2}$	
Global buckling	$\frac{\varepsilon_{\text{prestrain}}}{1+\varepsilon_{\text{prestrain}}} > \frac{\gamma HSL^2}{4Eh^3 b\lambda^2}$	$\frac{\varepsilon_{\text{prestrain}}}{1+\varepsilon_{\text{prestrain}}} > 3.8\frac{h^2H^2}{b^2L^2} + \sqrt{15\frac{h^4H^4}{b^4L^4} + 3.8\frac{\gamma H^3 S}{Ehb^3\lambda^2}}$

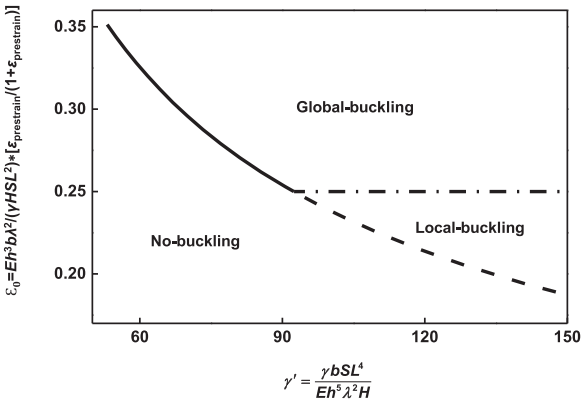

Fig. 5. The phase diagram of the normalized compression ε_0 versus the normalized adhesion energy γ' for no-, local- and global-buckling states.

2.5. Implications on the mechanics-guided, deterministic 3D assembly

As discussed in the introduction (Section 1), the mechanics-guided, deterministic 3D assembly prefers the global-buckling state. The results in Table 1 suggest two ways to facilitate this.

1) To achieve relatively weak adhesion $\gamma'=\frac{\gamma bSL^4}{Eh^5\lambda^2H}<92$ such that local-buckling never occurs. Considering $S=(\frac{\pi}{2}-1)b\lambda+2bH+2b^2$, it is clear that the decrease of adhesion energy γ, width b and representative length L, or increase of Young's modulus E, thickness h and unit cell length λ help to achieve global buckling. It is very sensitive to the thickness ($\propto h^{-5}$), representative length ($\propto L^4$) and width ($\propto b^2$ to b^3), is somewhat sensitive to the adhesion energy ($\propto\gamma$), Young's modulus ($\propto E^{-1}$) and unit cell length ($\propto\lambda^{-1}$ to λ^{-2}), and is insensitive to the height ($\propto 1$ to H^{-1}).
2) To reduce the critical compression $\frac{\gamma HSL^2}{4Eh^3b\lambda^2}$ for global buckling if the relatively strong adhesion is unavoidable $\gamma'=\frac{\gamma bSL^4}{Eh^5\lambda^2H}>92$. This suggests the decrease of adhesion energy γ, height H and representative length L, or increase of Young's modulus E, thickness h and unit cell length λ. It is very sensitive to the thickness ($\propto h^{-3}$) and representative length ($\propto L^2$), is somewhat sensitive to the adhesion energy ($\propto\gamma$), Young's modulus ($\propto E^{-1}$), unit cell length ($\propto\lambda^{-1}$ toλ^{-2}) and height ($\propto H$ to H^2), and is insensitive to the width ($\propto 1$ to b).

For both 1) and 2) above, the order of effectiveness to facilitate the global buckling is (i) increase of thickness h; (ii) decrease of representative length L; (iii) increase of unit cell length λ; and (iv) decrease of adhesion energy γ or increase of Young's modulus E. The decrease of width b and height H helps to prevent local buckling and to reduce the critical compression for global buckling, respectively.

3. The maximum strain in the serpentine structures

For globally-buckled serpentine structures (complete delamination of weak bonding), it is important to ensure that the maximum strain is below the threshold for failure, such as the yield strain for metallic materials.

3.1. A scaling law for the maximum equivalent strain

For the globally-buckled metallic serpentine structures, the maximum equivalent strain ε_{eq} must not exceed the yield strain (e.g., ~0.3%). In general, ε_{eq} is $\propto\kappa h$, where the curvature κ is $\propto L^{-1}$, and is also linearly proportional to the square root of the compression. These lead to the following scaling law

$$\varepsilon_{eq}=\frac{hb}{HL}F\left(\frac{b}{\lambda}\right)\sqrt{\frac{\varepsilon_{prestrain}}{1+\varepsilon_{prestrain}}} \tag{16}$$

for $h\ll b\ll L$, where the linear proportionality to H^{-1} is supported by FEA, and the function F is to be determined by FEA. Fig. 6a–c show ε_{eq} versus $\frac{hb}{HL}\sqrt{\frac{\varepsilon_{prestrain}}{1+\varepsilon_{prestrain}}}$ obtained by FEA for the wide ranges of h, b, H, L and $\varepsilon_{prestrain}$, and $\frac{b}{\lambda}=0.125$, 0.25 and 0.375[4]. The straight lines clearly validate the scaling law above, and their slopes give the function F, which, as shown versus $\frac{b}{\lambda}$ in Fig. 6d, has a minimal value ~20 when $b=0.3\lambda$. Therefore, the maximum equivalent strain is simply given by

[4] FEA is similar to that in Section 2 except that there are at least 25 elements along the width direction of the ribbon to ensure the accuracy.

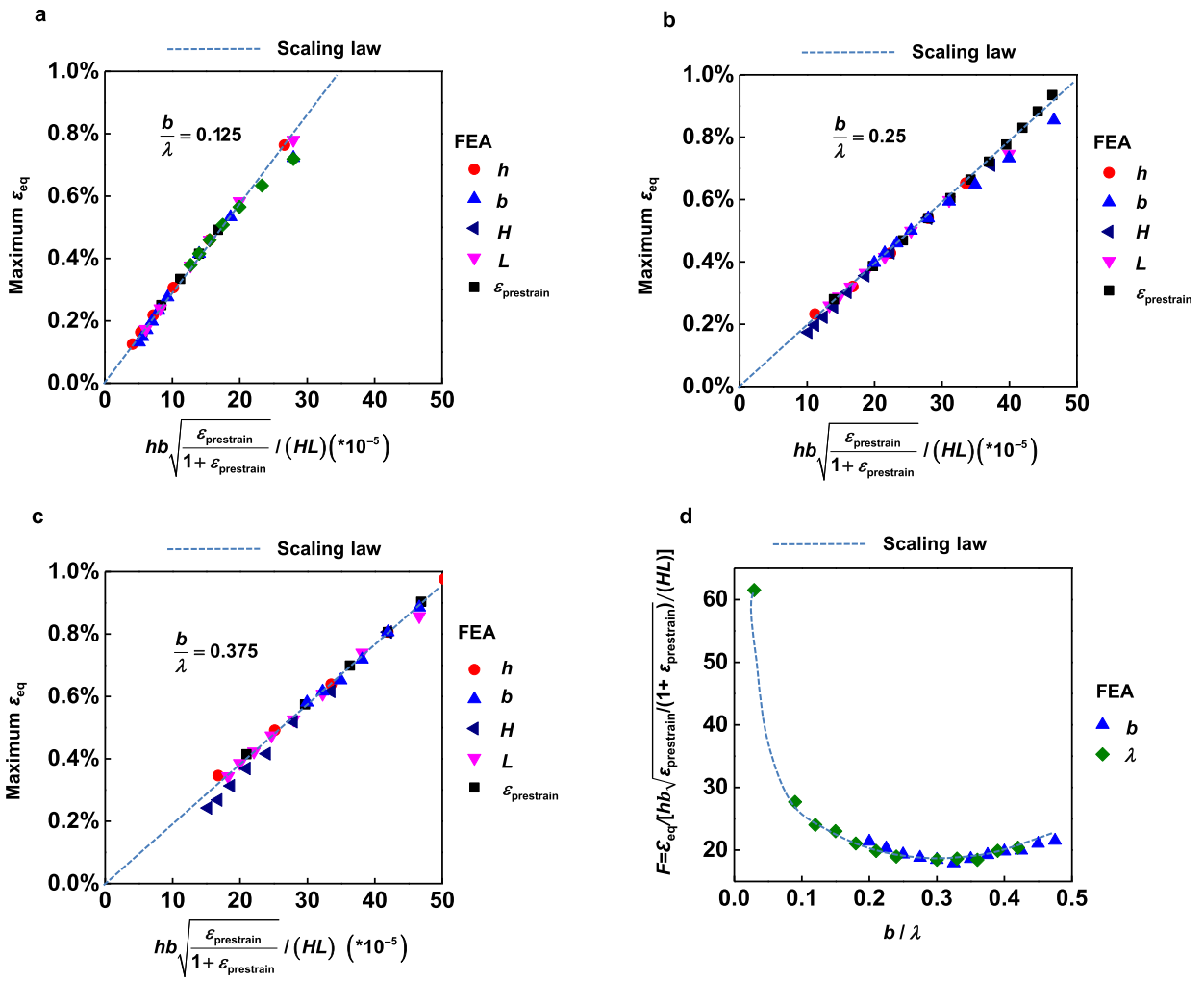

Fig. 6. (a)–(c) The scaling law for the maximum equivalent strain ε_{eq} in the buckled serpentine structure versus $hb\sqrt{\varepsilon_{prestrain}/(1+\varepsilon_{prestrain})}/(HL)$ for $b/\lambda = 0.125$, 0.25 and 0.375, respectively; and (d) the slope of the straight line in (a–c) versus b/λ.

$$\varepsilon_{eq} = 6\frac{h\lambda}{HL}\sqrt{\frac{\varepsilon_{prestrain}}{1+\varepsilon_{prestrain}}} \text{ for } b = 0.3\lambda. \tag{17}$$

It should be pointed out that ε_{eq} obtained by FEA is independent of the Young's Modulus E, and has a weak dependence (a few percent difference) on the Poisson's ratio. The Poisson's ratio in Fig. 6 is 0.34 (for Polyimide).

3.2. Optimal design of serpentine structures

For $b = 0.3\lambda$ from Eq. (17), the condition for relatively weak adhesion in Table 1 becomes

$$\frac{\gamma L^4}{Eh^5}\left(1+0.58\frac{\lambda}{H}\right) < 510. \tag{18}$$

Global bucking then occurs when the compression exceeds a critical value (obtained from Table 1)

$$\frac{\varepsilon_{prestrain}}{1+\varepsilon_{prestrain}} > 42\frac{h^2H^2}{\lambda^2L^2} + \sqrt{1.8\times10^3\frac{h^4H^4}{\lambda^4L^4} + 49\frac{\gamma H^3}{Eh\lambda^3} + 84\frac{\gamma H^4}{Eh\lambda^4}}$$
$$\text{for } \frac{\gamma L^4}{Eh^5}\left(1+0.58\frac{\lambda}{H}\right) < 510. \tag{19}$$

For relatively strong adhesion $\frac{\gamma L^4}{Eh^5}(1+0.58\frac{\lambda}{H})>510$, the critical compression to ensure global buckling in Table 1 becomes

$$\frac{\varepsilon_{\text{prestrain}}}{1+\varepsilon_{\text{prestrain}}}>\frac{\gamma H^2L^2}{2Eh^3\lambda^2}\left(1+0.58\frac{\lambda}{H}\right)\quad\text{for}\ \frac{\gamma L^4}{Eh^5}\left(1+0.58\frac{\lambda}{H}\right)>510. \tag{20}$$

Once global buckling is ensured by Eqs. (19) or (20), the maximum equivalent strain ε_{eq} in Eq. (17) can then be reduced by the decrease of thickness h, and increase of height H or the number of unit cells $\frac{L}{\lambda}$. For example, for the baseline values $E=2.5$ GPa, $h=10$ μm, λ=200 μm, $H=400$ μm, and $L=2000$ μm, and $b=60$ μm [satisfies $b=0.3\lambda$ in Eq. (17)], Eq. (19) becomes $\frac{\varepsilon_{\text{prestrain}}}{1+\varepsilon_{\text{prestrain}}}>0.11$ for $\gamma<0.0062$N/m, while Eq. (20) becomes $\frac{\varepsilon_{\text{prestrain}}}{1+\varepsilon_{\text{prestrain}}}>0.66$ for $\gamma>0.0062$N/m. The maximum equivalent strain ε_{eq} in Eq. (17) would increase (undesirably) by a factor of 2.5 if the semicircles are connected directly without the straight segment in the serpentine (then $H=\frac{\lambda}{2}+b$=160 μm). Similarly, ε_{eq} would increase (undesirably) by a factor of 2 if the number of unit cells decreases to $\frac{L}{\lambda}=5$.

4. Conclusion

Through theoretical modeling and FEA, this study produces a phase diagram of buckling states for serpentine structures formed via the mechanics-guided, deterministic 3D assembly. The phase diagram can be explicitly expressed by very concise formulae containing only two dimensionless combinations of parameters, i.e. the normalized compression ε_0 and the normalized adhesion γ', although originally there are eight parameters (five geometries, modulus, prestrain and work of adhesion) that come into play. The phase diagram clearly shows the means to facilitate the preferred global-buckling state in the mechanics-guided, deterministic 3D assembly (see Section 2.5).

A scaling law in explicit and concise form is developed for the maximum strain in the globally-buckled serpentine structures. The scaling law suggests that the optimized ratio of the serpentine width b over the unit cell length λ to minimize the maximum equivalent strain ε_{eq} is $b/\lambda=0.3$. Under this optimized geometry, $\varepsilon_{eq}$is linearly proportional to the geometry parameters and the prestrain in the combination $\frac{h\lambda}{HL}\sqrt{\frac{\varepsilon_{\text{prestrain}}}{1+\varepsilon_{\text{prestrain}}}}$. The scaling law clearly shows the means to keep the maximum strain below the threshold for failure (see Section 3.2).

In summary, the developed theoretical models may serve as design guidelines to the buckled serpentine structures with potential applications in stretchable electronics and 3D micro-electromechanical systems.

Acknowledgments

Y.Z. acknowledges the support from the National Natural Science Foundation of China (11722217) and the Tsinghua National Laboratory for Information Science and Technology. Y.H. acknowledges support from NSF (CMMI1635443).

Appendix A. The approximation of W_{local}

The ratio of the first to second terms of W_{local} in Eq. (7) is $1.9(\frac{h}{b})^2\frac{l}{L}(\frac{H}{L-l})^2$, which is on the order of $(\frac{h}{b})^2(\frac{H}{L})^2$ and is much less than 1 for $h\ll b$ and $H\ll L$. Fig. A1 shows the phase diagrams based on the exact and approximate W_{local} in Eq. (7) and Eq. (8), and their differences are only a few percent.

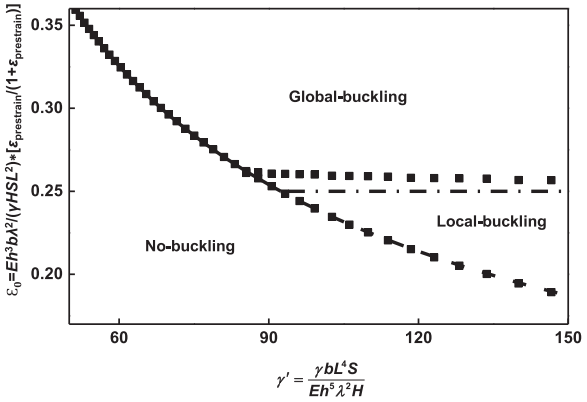

Fig. A1. The phase diagram of the normalized compression ε_0 versus the normalized adhesion energy γ' for no-, local- and global-buckling states. The lines and the dots are the approximate and the exact solutions, respectively.

References

Ahn, B.Y., Duoss, E.B., Motala, M.J., Guo, X., Park, S.-I., Xiong, Y., Yoon, J., Nuzzo, R.G., Rogers, J.A., Lewis, J.A., 2009. Omnidirectional printing of flexible, stretchable, and spanning silver microelectrodes. Science 323, 1590–1593.

Alcheikh, N., Shaikh, S.F., Hussain, M.M., 2018. Ultra-stretchable Archimedean interconnects for stretchable electronics. Extreme Mech. Lett. 24, 6–13.

Cao, H., Evans, A.G., 1993. Nonlinear deformation of ferroelectric ceramics. J. Am. Ceram. Soc. 76, 890–896.

Chen, H., Zhu, F., Jang, K.I., Feng, X., Rogers, J.A., Zhang, Y., Huang, Y., Ma, Y., 2018. The equivalent medium of cellular substrate under large stretching, with applications to stretchable electronics. J. Mech. Phys. Solids 120, 199–207.

Chen, Y., Liu, Y., Yan, Y., Zhu, Y., Chen, X., 2016. Helical coil buckling mechanism for a stiff nanowire on an elastomeric substrate. J. Mech. Phys. Solids 95, 25–43.

Coupeau, C., Boijoux, R., Ni, Y., Parry, G., 2019. Interacting straight-sided buckles: an enhanced attraction by substrate elasticity. J. Mech. Phys. Solids 124, 526–535.

Cui, Z., Han, Y., Huang, Q., Dong, J., Zhu, Y., 2018a. Electrohydrodynamic printing of silver nanowires for flexible and stretchable electronics. Nanoscale 10, 6806–6811.

Cui, J., Poblete, F.R., Zhu, Y., 2018b. Origami/kirigami-guided morphing of composite sheets. Adv. Funct. Mater. 28, 1802768.

Dai, X., Zhou, W., Gao, T., Liu, J., Lieber, C.M., 2016. Three-dimensional mapping and regulation of action potential propagation in nanoelectronics-innervated tissues. Nat. Nanotechnol. 11, 776–782.

Dong, W., Wang, Y., Zhou, Y., Bai, Y., Ju, Z., Guo, J., Gu, G., Bai, K., Ouyang, G., Chen, S., Zhang, Q., Huang, Y., 2018a. Soft human–machine interfaces: design, sensing and stimulation. Int. J. Intel. Robot. Appl. 2, 313–338.

Dong, W., Zhu, C., Hu, W., Xiao, L., Huang, Y., 2018b. Stretchable human-machine interface based on skin-conformal sEMG electrodes with self-similar geometry. J. Semicond. 39, 014001.

Fan, J.A., Yeo, W.H., Su, Y., Hattori, Y., Lee, W., Jung, S.Y., Zhang, Y., Liu, Z., Cheng, H., Falgout, L., Bajema, M., Coleman, T., Gregoire, D., Larsen, R.J., Huang, Y., Rogers, J.A., 2014. Fractal design concepts for stretchable electronics. Nat. Commun. 5, 3266.

Fan, Z., Hwang, K.-C., Rogers, J.A., Huang, Y., Zhang, Y., 2018. A double perturbation method of postbuckling analysis in 2D curved beams for assembly of 3D ribbon-shaped structures. J. Mech. Phys. Solids 111, 215–238.

Fu, H., Xu, S., Xu, R., Jiang, J., Zhang, Y., Rogers, J.A., Huang, Y., 2015. Lateral buckling and mechanical stretchability of fractal interconnects partially bonded onto an elastomeric substrate. Appl. Phys. Lett. 106, 091902.

Fu, H., Nan, K., Froeter, P., Huang, W., Liu, Y., Wang, Y., Wang, J., Yan, Z., Luan, H., Guo, X., Zhang, Y., Jiang, C., Li, L., Dunn, A.C., Li, X., Huang, Y., Zhang, Y., Rogers, J.A., 2017. Mechanically-guided deterministic assembly of 3D mesostructures assisted by residual stresses. Small 13, 1700151.

Fu, H., Nan, K., Bai, W., Huang, W., Bai, K., Lu, L., Zhou, C., Liu, Y., Liu, F., Wang, J., Han, M., Yan, Z., Luan, H., Zhang, Y., Zhang, Y., Zhao, J., Cheng, X., Li, M., Lee, J.W., Liu, Y., Fang, D., Li, X., Huang, Y., Zhang, Y., Rogers, J.A., 2018. Morphable 3D mesostructures and microelectronic devices by multistable buckling mechanics. Nat. Mater. 17, 268–276.

Gao, Y., Ota, H., Schaler, E.W., Chen, K., Zhao, A., Gao, W., Fahad, H.M., Leng, Y., Zheng, A., Xiong, F., Zhang, C., Tai, L.-C., Zhao, P., Fearing, R.S., Javey, A., 2017a. Wearable microfluidic diaphragm pressure sensor for health and tactile touch monitoring. Adv. Mater. 29, 1701985.

Gao, Y., Zhang, Y., Wang, X., Sim, K., Liu, J., Chen, J., Feng, X., Xu, H., Yu, C., 2017b. Moisture-triggered physically transient electronics. Sci. Adv. 3, e1701222.

Guillon, O., Thiebaud, F., Perreux, D., 2002. Tensile fracture of soft and hard PZT. Int. J. Fract. 117, 235–246.

Guo, X., Wang, X., Ou, D., Ye, J., Pang, W., Huang, Y., Rogers, J.A., Zhang, Y., 2018a. Controlled mechanical assembly of complex 3D mesostructures and strain sensors by tensile buckling. npj Flex. Elec. 2, 14.

Guo, X., Xu, Z., Zhang, F., Wang, X., Zi, Y., Rogers, J.A., Huang, Y., Zhang, Y., 2018b. Reprogrammable 3D mesostructures through compressive buckling of thin films with prestrained shape memory polymer. Acta Mech. Solida Sin. 31, 589–598.

Gutruf, P., Walia, S., Ali, M.N., Sriram, S., Bhaskaran, M., 2014. Strain response of stretchable micro-electrodes: controlling sensitivity with serpentine designs and encapsulation. Appl. Phys. Lett. 104, 021908.

Gutruf, P., Krishnamurthi, V., Vázquez-Guardado, A., Xie, Z., Banks, A., Su, C.-J., Xu, Y., Haney, C.R., Waters, E.A., Kandela, I., Krishnan, S.R., Ray, T., Leshock, J.P., Huang, Y., Chanda, D., Rogers, J.A., 2018. Fully implantable optoelectronic systems for battery-free, multimodal operation in neuroscience research. Nat. Elec. 1, 652–660.

Han, S., Kim, M.K., Wang, B., Wie, D.S., Wang, S., Lee, C.H., 2016. Mechanically reinforced skin-electronics with networked nanocomposite elastomer. Adv. Mater. 28, 10257–10265.

Han, M., Wang, H., Yang, Y., Liang, C., Bai, W., Yan, Z., Li, H., Xue, Y., Wang, X., Akar, B., Zhao, H., Luan, H., Lim, J., Kandela, I., Ameer, G.A., Zhang, Y., Huang, Y., Rogers, J.A., 2019. Three-dimensional piezoelectric polymer microsystems for vibrational energy harvesting, robotic prosthetic interfaces, and biomedical implants. Nat. Elec. 2, 26–35.

Hu, H., Zhu, X., Wang, C., Zhang, L., Li, X., Lee, S., Huang, Z., Chen, R., Chen, Z., Wang, C., Gu, Y., Teng, Y., Zhou, W., Li, Y., Nomoto, A., Sternini, S., Zhou, Q., Pharr, M., Scalea, F.L.D., Xu, S., 2018. Stretchable ultrasonic transducer arrays for three-dimensional imaging on complex surfaces. Sci. Adv. 4, eaar3979.

Huang, Y., Ding, Y., Bian, J., Su, Y., Zhou, J., Duan, Y., Yin, Z., 2017. Hyper-stretchable self-powered sensors based on electrohydrodynamically printed, self-similar piezoelectric nano/microfibers. Nano Energy 40, 432–439.

Jang, K.-I., Li, K., Chung, H.U., Xu, S., Jung, H.N., Yang, Y., Kwak, J.W., Jung, H.H., Song, J., Yang, C., Wang, A., Liu, Z., Lee, J.Y., Kim, B.H., Kim, J.H., Lee, J., Yu, Y, Kim, B.J., Jang, H., Yu, K.J., Kim, J., Lee, J.W., Jeong, J.-W., Song, Y.M., Huang, Y., 2017. Self-assembled three dimensional network designs for soft electronics. Nat. Commun. 8, 15894.

Khang, D.-Y., Jiang, H., Huang, Y., Rogers, J.A., 2006. A stretchable form of single-crystal silicon for high-performance electronics on rubber substrates. Science 311, 208–212.

Kim, Y., Yuk, H., Zhao, R., Chester, S.A., Zhao, X., 2018a. Printing ferromagnetic domains for untethered fast-transforming soft materials. Nature 558, 274–279.

Kim, B.H., Lee, J., Won, S.M., Xie, Z., Chang, J.K., Yu, Y., Cho, Y.K., Jang, H., Jeong, J.Y., Lee, Y., Ryu, A., Kim, D.H., Lee, K.H., Lee, J.Y., Liu, F., Wang, X., Huo, Q., Min, S., Wu, D., Ji, B., Banks, A., Kim, J., Oh, N., Jin, H.M., Han, S., Kang, D., Lee, C.H., Song, Y.M., Zhang, Y., Huang, Y., Jang, K.-I., Rogers, J.A., 2018b. Three-dimensional silicon electronic systems fabricated by compressive buckling process. ACS Nano 12, 4164–4171.

Kim, B.H., Liu, F., Yu, Y., Jang, H., Xie, Z., Li, K., Lee, J., Jeong, J.Y., Ryu, A., Lee, Y., Kim, D.H., Wang, X., Lee, K., Lee, J.Y., Won, S.M., Oh, N., Kim, J., Kim, J.Y., Jeong, S.J., Jang, K.-I., Lee, S., Huang, Y., Zhang, Y., Rogers, J.A., 2018c. Mechanically guided post-assembly of 3D electronic systems. Adv. Funct. Mater. 28, 1803149.

Kolesky, D.B., Truby, R.L., Gladman, A.S., Busbee, T.A., Homan, K.A., Lewis, J.A., 2014. 3D bioprinting of vascularized, heterogeneous cell-laden tissue constructs. Adv. Mater. 26, 3124–3130.

Lai, Y.C., Deng, J., Zhang, S.L., Niu, S., Guo, H., Wang, Z.L., 2017. Single-thread-based wearable and highly stretchable triboelectric nanogenerators and their applications in cloth-based self-powered human-interactive and biomedical sensing. Adv. Funct. Mater. 27, 1604462.

Li, H., Wang, X., Zhu, F., Ning, X., Wang, H., Rogers, J.A., Zhang, Y., Huang, Y., 2018a. Viscoelastic characteristics of mechanically assembled three-dimensional structures formed by compressive buckling. J. Appl. Mech. Trans. ASME 85, 121002.

Li, K., Wu, W., Jiang, Z., Cai, S., 2018b. Voltage-induced wrinkling in a constrained annular dielectric elastomer film. J. Appl. Mech. Trans. ASME 85, 011007.

Liao, X., Xiao, J., Ni, Y., Li, C., Chen, X., 2017. Self-assembly of islands on spherical substrates by surface instability. ACS Nano 11, 2611–2617.

Lin, S., Yuk, H., Zhang, T., Parada, G.A., Koo, H., Yu, C., Zhao, X., 2016. Stretchable hydrogel electronics and devices. Adv. Mater. 28, 4497–4505.

Liu, Y., Yan, Z., Lin, Q., Guo, X., Han, M., Nan, K., Hwang, K.C., Huang, Y., Zhang, Y., Rogers, J.A., 2016. Guided formation of 3D helical mesostructures by mechanical buckling: analytical modeling and experimental validation. Adv. Funct. Mater. 26, 2909–2918.

Liu, Y., Pharr, M., Salvatore, G.A., 2017. Lab-on-skin: a review of flexible and stretchable electronics for wearable health monitoring. ACS Nano 11, 9614–9635.

Lu, N., Lu, C., Yang, S., Rogers, J.A., 2012. Highly sensitive skin-mountable strain gauges based entirely on elastomers. Adv. Funct. Mater. 22, 4044–4050.

Lu, N., Kim, D.H., 2014. Flexible and stretchable electronics paving the way for soft robotics. Soft Robot 1, 53–62.
Lu, N., Yang, S., 2015. Mechanics for stretchable sensors. Curr. Opin. Solid St. Mater. 19, 149–159.
Ma, Q, Zhang, Y., 2016. Mechanics of fractal-inspired horseshoe microstructures for applications in stretchable electronics. J. Appl. Mech. Trans. ASME 83, 111008.
Ma, Y., Feng, X., Rogers, J.A., Huang, Y., Zhang, Y., 2017a. Design and application of 'J-shaped' stress–strain behavior in stretchable electronics: a review. Lab Chip 17, 1689–1704.
Ma, Y., Pharr, M., Wang, L., Kim, J., Liu, Y., Xue, Y., Ning, R., Wang, X., Chung, H.U., Feng, X., Rogers, J.A., Huang, Y., 2017b. Soft elastomers with ionic liquid-filled cavities as strain isolating substrates for wearable electronics. Small 13, 1602954.
Mamidanna, A., Song, Z., Lv, C., Lefky, C.S., Jiang, H., Hildreth, O.J., 2016. Printing stretchable spiral interconnects using reactive ink chemistries. ACS Appl. Mater. Interfaces 8, 12594–12598.
Mao, G., Wu, L., Liang, X., Qu, S., 2017. Morphology of voltage-triggered ordered wrinkles of a dielectric elastomer sheet. J. Appl. Mech. Trans. ASME 84, 111005.
Nan, K., Wang, H., Ning, X., Miller, K.A., Wei, C., Liu, Y., Li, H., Xue, Y., Xie, Z., Luan, H., Zhang, Y., Huang, Y., Rogers, J.A., Braun, P.V., 2018a. Soft 3D microscale vibratory platforms for characterization of nano-thin polymer films. ACS Nano doi:10.1021/acsnano.8b06736.
Nan, K., Kang, S.D., Li, K., Yu, K.J., Zhu, F., Wang, J., Dunn, A.C., Zhou, C., Xie, Z., Agne, M.T., Wang, H., Luan, H., Zhang, Y., Huang, Y., Snyder, G.J., Rogers, J.A., 2018b. Compliant and stretchable thermoelectric coils for energy harvesting in miniature flexible devices. Sci. Adv. 4, eaau5849.
Ning, X., Wang, H., Yu, X., Soares, J.A., Yan, Z., Nan, K., Velarde, G., Xue, Y., Sun, R., Dong, Q., Luan, H., Lee, C.M., Chempakasseril, A., Han, M., Wang, Y., Li, L., Huang, Y., Zhang, Y., Rogers, J.A., 2017. 3D tunable, multiscale, and multistable vibrational micro-platforms assembled by compressive buckling. Adv. Funct. Mater. 27, 1605914.
Ning, X., Yu, X., Wang, H., Sun, R., Corman, R., Li, H., Lee, C.M., Xue, Y., Chempakasseril, A., Yao, Y., Zhang, Z., Luan, H., Wang, Z., Xia, W., Feng, X., Ewoldt, R.H., Huang, Y., Zhang, Y., Rogers, J.A., 2018a. Mechanically active materials in three-dimensional mesostructures. Sci. Adv. 4, eaat8313.
Ning, X., Wang, X., Zhang, Y., Yu, X., Choi, D., Zheng, N., Kim, D.S., Huang, Y., Zhang, Y., Rogers, J.A., 2018b. Assembly of advanced materials into 3D functional structures by methods inspired by origami and kirigami: a review. Adv. Mater. Interfaces 5, 1800284.
Nyein, H.Y.Y., Tai, L.C., Ngo, Q.P., Chao, M., Zhang, G., Gao, W., Bariya, M., Bullock, J., Kim, H., Fahad, H.M., Javey, A., 2018. A wearable sweat sensing patch for dynamic sweat secretion analysis. ACS Sens. 3, 944–952.
Pan, T., Pharr, M., Ma, Y., Ning, R., Yan, Z., Xu, R., Feng, X., Huang, Y., Rogers, J.A., 2017. Experimental and theoretical studies of serpentine interconnects on ultrathin elastomers for stretchable electronics. Adv. Funct. Mater. 27, 1702589.
Park, S.I., Brenner, D.S., Shin, G., Morgan, C.D., Copits, B.A., Chung, H.U., Pullen, M.Y., Noh, K.N., Davidson, S., Oh, S.J., Yoon, J., Jang, K.I., Samineni, V.K., Norman, M, Grajales-Reyes, J.G., Vogt, S.K., Sundaram, S.S., Wilson, K.M., Ha, J.S., Xu, R., Pan, T., Kim, T.i., Huang, Y., Montana, M.C., Golden, J.P., Bruchas, M.R., Gereau IV, R.W., Rogers, J.A., 2015. Soft, stretchable, fully implantable miniaturized optoelectronic systems for wireless optogenetics. Nat. Biotechnol. 33, 1280–1286.
Shi, X., Xu, R., Li, Y., Zhang, Y., Ren, Z., Gu, J., Rogers, J.A., Huang, Y., 2014. Mechanics design for stretchable, high areal coverage GaAs solar module on an ultrathin substrate. J. Appl. Mech. Trans. ASME 81, 124502.
Skylar-Scott, M.A., Gunasekaran, S., Lewis, J.A., 2016. Laser-assisted direct ink writing of planar and 3D metal architectures. Proc. Natl. Acad. Sci. USA 113, 6137–6142.
Son, D., Lee, J., Qiao, S., Ghaffari, R., Kim, J., Lee, J.E., Song, C., Kim, S.J., Lee, D.J., Jun, S.W., Yang, S., Park, M., Shin, J., Do, K., Lee, M., Kang, K., Hwang, C.S., Lu, N., Hyeon, T., Kim, D.H., 2014. Multifunctional wearable devices for diagnosis and therapy of movement disorders. Nat. Nanotechnol. 9, 397–404.
Su, Y., Wu, J., Fan, Z., Hwang, K.-C., Song, J., Huang, Y., Rogers, J.A., 2012. Postbuckling analysis and its application to stretchable electronics. J. Mech. Phys. Solids 60, 487–508.
Su, Y., Ping, X., Yu, K.J., Lee, J.W., Fan, J.A., Wang, B., Li, M., Li, R., Harburg, D.V., Huang, Y., Yu, C., Mao, S., Shim, J., Yang, Q., Lee, P.-Y., Armonas, A., Choi, K.-J., Yang, Y., Paik, U., Chang, T., Dawidczyk, T.J., Huang, Y., Wang, S., Rogers, J.A., 2017. In-plane deformation mechanics for highly stretchable electronics. Adv. Mater. 29, 1604989.
Sun, L., Parker, S.T., Syoji, D., Wang, X., Lewis, J.A., Kaplan, D.L., 2012. Direct-write assembly of 3D silk/hydroxyapatite scaffolds for bone co-cultures. Adv. Healthcare Mater. 1, 729–735.
Sun, Y., Choi, W.M., Jiang, H., Huang, Y., Rogers, J.A., 2006. Controlled buckling of semiconductor nanoribbons for stretchable electronics. Nat. Nanotechnol. 1, 201–207.
Vásquez Quintero, A., Verplancke, R., De Smet, H., Vanfleteren, J., 2017. Stretchable electronic platform for soft and smart contact lens applications. Adv. Mater. Technol. 2, 1700073.
Vedde, J., Gravesen, P., 1996. The fracture strength of nitrogen doped silicon wafers. Mater. Sci. Eng. B 36, 246–250.
Vella, D., Bico, J., Boudaoud, A., Roman, B., Reis, P.M., 2009. The macroscopic delamination of thin films from elastic substrates. Proc. Natl. Acad. Sci. USA 106, 10901–10906.
Wang, B., Wang, S., 2016. Adhesion-governed buckling of thin-film electronics on soft tissues. J. Theor. App. Mech. Pol. 6, 6–10.
Wang, B., Bao, S., Vinnikova, S., Ghanta, P., Wang, S., 2017. Buckling analysis in stretchable electronics. npj Flex. Elec. 1, 5.
Wang, H., Ning, X., Li, H., Luan, H., Xue, Y., Yu, X., Fan, Z., Li, L., Rogers, J.A., Zhang, Y., Huang, Y., 2018. Vibration of mechanically-assembled 3D microstructures formed by compressive buckling. J. Mech. Phys. Solids 112, 187–208.
Wang, X., Guo, X., Ye, J., Zheng, N., Kohli, P., Choi, D., Zhang, Y., Xie, Z., Zhang, Q., Luan, H., Nan, K., Kim, B.H., Xu, Y., Shan, X., Bai, W., Sun, R., Wang, Z., Jang, H., Zhang, F., Ma, Y., Xu, Z., Feng, X., Xie, T., Huang, Y., Zhang, Y., Rogers, J.A., 2019. Freestanding 3D mesostructures, functional devices, and shape-programmable systems based on mechanically induced assembly with shape memory polymers. Adv. Mater. 31, 1805615. https://doi.org/10.1002/adma.201805615.
Wang, S., Xiao, J., Song, J., Ko, H.C., Hwang, K.-C., Huang, Y., Rogers, J.A., 2010. Mechanics of curvilinear electronics. Soft Matter 6, 5757–5763.
Wehner, M., Truby, R.L., Fitzgerald, D.J., Mosadegh, B., Whitesides, G.M., Lewis, J.A., Wood, R.J., 2016. An integrated design and fabrication strategy for entirely soft, autonomous robots. Nature 536, 451–455.
Wu, W., DeConinck, A., Lewis, J.A., 2011. Omnidirectional printing of 3D microvascular networks. Adv. Mater. 23, H178–H183.
Xiao, J., Jiang, H., Khang, D.Y., Wu, J., Huang, Y., Rogers, J.A., 2008. Mechanics of buckled carbon nanotubes on elastomeric substrates. J. Appl. Phys. 104, 033543.
Xu, S., Zhang, Y., Cho, J., Lee, J., Huang, X., Jia, L., Fan, J.A., Su, Y., Su, J., Zhang, H., Cheng, H., Lu, B., Yu, C., Chuang, C., Kim, T.-I., Song, T., Shigeta, K., Kang, S., Dagdeviren, C., Petrov, I., Braun, P.V., Huang, Y., Paik, U., Rogers, J.A., 2013. Stretchable batteries with self-similar serpentine interconnects and integrated wireless recharging systems. Nat. Commun. 4, 1543.
Xu, S., Zhang, Y., Jia, L., Mathewson, K.E., Jang, K.I., Kim, J., Fu, H., Huang, X., Chava, P., Wang, R., Bhole, S., Wang, L., Na, Y.J., Guan, Y., Flavin, M., Han, Z., Huang, Y., Rogers, J.A., 2014. Soft microfluidic assemblies of sensors, circuits, and radios for the skin. Science 344, 70–74.
Xu, S., Yan, Z., Jang, K.-I., Huang, W., Fu, H., Kim, J., Wei, Z., Flavin, M., McCracken, J., Wang, R., Badea, A., Liu, Y., Xiao, D., Zhou, G., Lee, J., Chung, H.U., Cheng, H., Ren, W., Banks, A., Li, X., Paik, U., Nuzzo, R.G., Huang, Y., Zhang, Y., Rogers, J.A., 2015. Assembly of micro/nanomaterials into complex, three-dimensional architectures by compressive buckling. Science 347, 154–159.
Xue, Y., Lee, W.-K., Yuan, J., Odom, T.W., Huang, Y., 2018. Mechanics modeling of hierarchical wrinkle structures from sequential release of prestrain. Langmuir doi:10.1021/acs.langmuir.8b03498.
Yan, Z., Zhang, F., Liu, F., Han, M., Ou, D., Liu, Y., Lin, Q., Guo, X., Fu, H., Xie, Z., Gao, M., Huang, Y., Kim, J., Qiu, Y., Nan, K., Kim, J., Gutruf, P., Luo, H., Zhao, A., Hwang, K.C., Huang, Y., Zhang, Y., Rogers, J.A., 2016. Mechanical assembly of complex, 3D mesostructures from releasable multilayers of advanced materials. Sci. Adv. 2, e1601014.

Yan, Z., Han, M., Shi, Y., Badea, A., Yang, Y., Kulkarni, A., Hanson, E., Kandel, M.E., Wen, X., Zhang, F., Luo, Y., Lin, Q., Zhang, H., Guo, X., Huang, Y., Nan, K., Jia, S., Oraham, A.W., Mevis, M.B., Lim, J., Guo, X., Gao, M., Ryu, W., Yu, K.J., Nicolau, B.G., Petronico, A., Rubakhin, S.S., Lou, J., Ajayan, P.M., Thornton, K., Popescu, G., Fang, D., Sweedler, J.V., Braun, P.V., Zhang, H., Nuzzo, R.G., Huang, Y., Zhang, Y., Rogers, J.A., 2017. Three-dimensional mesostructures as high-temperature growth templates, electronic cellular scaffolds, and self-propelled microrobots. Proc. Natl. Acad. Sci. USA 114, E9455–E9464.

Yang, P.-K., Lin, L., Yi, F., Li, X., Pradel, K.C., Zi, Y., Wu, C.-I., He, J.-H., Zhang, Y., Wang, Z., 2015. A flexible, stretchable and shape-adaptive approach for versatile energy conversion and self-powered biomedical monitoring. Adv. Mater. 27, 3817–3824.

Yang, Y., Vervust, T., Dunphy, S., Van Put, S., Vandecasteele, B., Dhaenens, K., Degrendele, L., Mader, L., Vriese, L.D., Martens, T., Kaufmann, M., Sekitani, T., Vanfleteren, J., 2018. 3D multifunctional composites based on large-area stretchable circuit with thermoforming technology. Adv. Elec. Mater. 1800071.

Yu, S., Sun, Y., Li, S., Ni, Y., 2018. Harnessing fold-to-wrinkle transition and hierarchical wrinkling on soft material surfaces by regulating substrate stiffness and sputtering flux. Soft Matter 14, 6745–6755.

Zarek, M., Layani, M., Cooperstein, I., Sachyani, E., Cohn, D., Magdassi, S., 2016. 3D printing of shape memory polymers for flexible electronic devices. Adv. Mater. 28, 4449–4454.

Zhang, F., Liu, F., Zhang, Y., 2019. Analyses of mechanically-assembled 3D spiral mesostructures with applications as tunable inductors. Sci. China Technol. Sci.. https://doi.org/10.1007/s11431-018-9368-y.

Zhang, Y., Fu, H., Su, Y., Xu, S., Cheng, H., Fan, J.A., Hwang, K.-C., Rogers, J.A., Huang, Y., 2013. Mechanics of ultra-stretchable self-similar serpentine interconnects. Acta Mater. 61, 7816–7827.

Zhang, Y., Wang, S., Li, X., Fan, J.A., Xu, S., Song, Y.M., Choi, K.J., Yeo, W.-H., Lee, W., Nazaar, S.N., Lu, B., Yin, L, Hwang, K.-C., Rogers, J.A., Huang, Y., 2014a. Experimental and theoretical studies of serpentine microstructures bonded to prestrained elastomers for stretchable electronics. Adv. Funct. Mater. 24, 2028–2037.

Zhang, Y., Fu, H., Xu, S., Fan, J.A., Hwang, K.-C., Jiang, J., Rogers, J.A., Huang, Y., 2014b. A hierarchical computational model for stretchable interconnects with fractal-inspired designs. J. Mech. Phys. Solids 72, 115–130.

Zhang, Y., Yan, Z., Nan, K., Xiao, D., Liu, Y., Luan, H., Fu, H., Wang, X., Yang, Q., Wang, J., Ren, W., Si, H., Liu, F., Yang, L., Li, H., Wang, J., Guo, X., Luo, H., Wang, L., Huang, Y., Rogers, J.A., 2015. A mechanically driven form of kirigami as a route to 3D mesostructures in micro/nanomembranes. Proc. Natl. Acad. Sci. USA 112, 11757–11764.

Zhang, Y., Zhang, F., Yan, Z., Ma, Q., Li, X., Huang, Y., Rogers, J.A., 2017. Printing, folding and assembly methods for forming 3D mesostructures in advanced materials. Nat. Rev. Mater. 2, 17019.

Zhao, Q., Liang, Z., Lu, B., Chen, Y., Ma, Y., Feng, X., 2018. Toothed substrate design to improve stretchability of serpentine interconnect for stretchable electronics. Adv. Mater. Technol. 3, 1800169.

Zhou, H., Qin, W., Yu, Q., Chen, F., Yu, X., Cheng, H., Wu, H., 2018. Controlled buckling and postbuckling behaviors of thin film devices suspended on an elastomeric substrate with trapezoidal surface relief structures. Int. J. Solids Struct. 160, 96–102. https://doi.org/10.1016/j.ijsolstr.2018.10.018.

Zhu, J., Cheng, H., 2018. Recent development of flexible and stretchable antennas for bio-integrated electronics. Sensors 18, 4364.